Soft Matter



PAPER



Cite this: *Soft Matter,* 2019, **15**. 5951

Received 1st April 2019, Accepted 26th June 2019

DOI: 10.1039/c9sm00658c

rsc.li/soft-matter-journal

Mechanical behavior of nonwoven non-crosslinked fibrous mats with adhesion and friction

V. Negi and R. C. Picu *

We present a study of the mechanical behavior of planar fibrous mats stabilized by inter-fiber adhesion. Fibers of various degrees of tortuosity and of infinite and finite length are considered in separate models. Fibers are randomly distributed, are not cross-linked, and interact through adhesion and friction. The variation of structural parameters such as the mat thickness and the mean segment length between contacts along given fibers with the strength of adhesion is determined. These systems are largely dissipative in that most of the work performed during deformation is dissipated frictionally and only a small fraction is stored as strain energy. The response of the mats to tensile loading has three regimes: a short elastic regime in which no sliding at contacts is observed, a well-defined sliding regime characterized by strain hardening, and a rapid stiffening regime at larger strains. The third regime is due to the formation of stress paths after the fiber tortuosity is pulled out and is absent in mats of finite length fibers. Networks of finite length fibers lose stability during the second regime of deformation. The scaling of the yield stress, which characterizes the transition between the first and the second regimes, and of the second regime's strain hardening modulus, with system parameters such as the strength of adhesion and friction and the degree of fiber tortuosity are determined. The strength of mats of finite length fibers is also determined as a function of network parameters. These results are expected to become useful in the design of electrospun mats and other planar fibrous non-cross-linked networks.

1. Introduction

Fiber networks form the key microstructural component of many soft biological and man-made materials. Collagen fibers form athermal network structures providing strength to the extra-cellular matrix (ECM) and to connective tissues in animals. F-actin networks and microtubules are structural components of the cytoskeleton in eukaryotic cells. Networks of various polymeric nanofibers, like polyacrylonitrile (PAN), poly-t-lactide (PLLA), poly-propylene (PP) etc., are used in applications like textiles, filtration, hygiene products, and tissue engineering. The abundance of examples of soft materials whose mechanics is controlled by a network is due to the superior specific properties (per unit weight of network materials) of such structures.

Crosslinked athermal fiber networks with inter-fiber permanent bonds have been studied extensively, as reviewed in ref. 1 and 2. Such networks show mechanical response dependent on whether the strain energy is stored predominantly in the bending or axial deformation modes of fibers. High network density, ρ , and high

Department of Mechanical, Aerospace and Nuclear Engineering, Rensselaer Polytechnic Institute, Troy, NY 12180, USA. E-mail: picuc@rpi.edu; Tel: +1-518-276-2195 fiber axial stiffness result in stiff, affine, axial energy-dominated, and mostly linear response. However, a highly nonlinear, bending dominated, and non-affine response is obtained at low network densities ρ . The nature of the inter-fiber bonds, *i.e.* rigid, pin-jointed or flexible, also influences the mechanical properties of fiber networks.

Less understood are the properties of non-crosslinked fiber networks with non-bonded interactions such as excluded volume, adhesion, and friction. Non-crosslinked networks can be woven or non-woven. Woven networks, like textiles, have patterned layouts of fibers designed to enhance (predominantly frictional) inter-fiber interactions. Nonwoven networks have random layouts of fibers. Electrospinning has been widely used to produce planar mats of nonwoven fiber networks of various polymeric materials, fiber diameters, and fiber tortuosity.³⁻⁶ These networks have found multiple applications. When used in tissue engineering, as scaffolds, the networks must be biocompatible and should have mechanical properties similar to those of the ECM.^{3,7} Thus, it is important to establish the structure–property relationship for these nonbonded networks in order to achieve control of their properties.

Electrospun nanofibrous mats typically show in tension a bilinear stress-strain response, with an initial linear regime,

a knee-region of yielding transition, and a long strain-hardening plastic regime of constant slope. ^{3,5,8–10} Their small-strain elastic modulus is weakly dependent on the fiber diameter. ^{9,10} Increasing fiber diameter is found to decrease the yield stress and the tangent slope in the strain-hardening plastic region (also termed the strain-hardening modulus), but increases the strain-to-failure. ^{9,10} Heat treatment leading to fusion of fibers at contacts and chemical crosslinking ¹¹ of such electrospun mats dramatically increases the small-strain modulus, the yield stress, and the strain-hardening modulus, but reduces the failure strain at the same time. This indicates that the physics of deformation and stress production changes upon network crosslinking.

Cellulose nanofibrillar (CNF) sheets (cellulose nanopaper) exhibit similar bi-linear behavior. 12 Their linear elastic response lasts up to 0.2-0.3% strain, followed by a long strain-hardening inelastic regime which extends up to $\sim 10\%$ strain. 12-15 Henriksson et al. 14 reported that decreasing the porosity of CNF nanopaper increases the small-strain elastic modulus, the yield stress, the strain-hardening modulus, and the failure stress, while the yield and failure strains remain largely unaffected. Zhu et al. 15 reported a sharp increase of the failure stress and strain when decreasing the fiber diameter from 27 µm to 11 nm, while maintaining the fiber density of the mats in the range of 1.2-0.8 g cm⁻³. An experimental study by Benítez et al.16 revealed that increasing the relative humidity decreases the small-strain modulus, the yield stress and the strain-hardening modulus. On the other hand, dry CNF nanopaper showed negligible inelasticity. Mao et al. 13 used Digital Image Correlation to study the deformation of the nanopaper during loading and found the deformation to be homogeneous during the strain-hardening inelastic regime. Several mechanisms have been proposed to explain the post-yield regime including slippage at contacts assisted by the breakage and reformation of hydrogen bonds, 14-16 and molecular mechanisms at the level of individual cellulose nanofibers. 13

Semi-analytical¹⁷ and numerical finite element (FE) based analyses 18-20 have attributed the elastic-plastic response of crosslinked nanofibrous mats to the elastic-plastic behavior of their constituent fibers. Zündel et al.20 developed a 3D model of quasiplanar electrospun mats with crosslinks between fibers. The stress-strain response observed is bilinear owing to the elasticplastic fiber constitutive properties. Goutianos et al. 21 modeled the stress-strain response of cellulose nanopaper 3D fibrous mats with breakable bonds and elastic-plastic fiber constitutive behavior. The response observed was brittle and it was found that, for the values of bond strength considered,21 fibers do not undergo yielding before mat fracture. Liu and Dzenis²² explored the mechanics of sparse electrospun mats with straight, non-bonded fibers running boundary-to-boundary, with Coulombic inter-fiber friction. This configuration leads to affine behavior, independent of the fiber properties, and, as expected, it was found that the mat-scale plasticity is associated with the plastic deformation of fibers.

The effect of excluded volume interactions (contacts between fibers) in non-crosslinked networks has been studied. A theoretical treatment of the compression of non-crosslinked elastic fiber networks without inter-fiber friction or adhesion is reported in ref. 23–25. It is found that the compressive stress increases rapidly,

as a power function of the fiber volume fraction, due to the increase of the number density of contacts. Experimental results support this observation. ^{26,27} Numerical analyses using the bead-spring model^{28,29} and FE representations of the fibers³⁰ also indicate rapid stiffening in compression. Hysteresis during compression cycles is observed when inter-fiber friction is present, or if fibers re-arrange during the cyclic loading.

Adhesion in fiber networks governs both network morphology and mechanics. Adhesion may drive fibers to self-organize into bundles, which form a network of bundles on larger scales. Such structural changes have been observed in carbon nanotube (CNT) networks, 31 collagen, 32 and actin filaments. 33 Numerical studies of the self-assembly of nonbonded fibers in ref. 34 reveal that when the strength of adhesion is high enough to overcome the strain energy penalty of fiber self-assembly, cellular networks of bundles, with bundle branching and merging, are formed. In the case of cross-linked networks, adhesive interactions lead to network shrinkage. 35 In such cases, adhesion stabilizes the structure of pre-stressed, highly bent fibers. Their mechanical behavior is quite different from that of cross-linked networks without adhesion.

Structural self-organization is inhibited by inter-fiber friction.³⁶ In such cases, adhesion stabilizes the fiber-fiber contacts and may act as a compacting force. Kulachenko and Uesaka³⁰ performed a 3D beam-to-beam contact FE-based numerical study to investigate the small strain response and failure behavior of finite-length fiber planar mats with excluded volume, adhesion, and friction interactions. Deformation localizes at small strains (1–2%) leading to strain softening, but a friction-stabilized post-localization response which extends to larger strains is observed. The effect of fiber crimp was found to be negligible at modest crimp values.

Crimp, also known as fiber tortuosity, is an important structural feature of random fiber networks. It is known to exist in collagen *in vivo*, ^{37,38} while most nonwoven fibrous materials made through processes like electrospinning have tortuous fibers. ^{3,5} The effect of crimp on the mechanics of cross-linked fiber networks has been studied numerically in ref. 39 and 40 and experimentally in ref. 39. In cross-linked networks, crimp decreases the small-strain elastic modulus, while the functional form of the large strain response is independent of crimp. ⁴⁰ Chao *et al.*⁵ synthesized and mechanically tested electrospun mats with crimped poly-L-lactic acid (PLLA) fibers. They report a decrease of the yield stress with increasing levels of fiber crimp. However, the post-yield strain-hardening modulus is found to increase with increasing crimp. ⁵

These studies show that the physics of non-woven and non-bonded fibrous mats is governed by interactions such as excluded volume, adhesion, and friction. In these systems, crimp (fiber waviness) and the fiber bending stiffness play an important role. However, a comprehensive description relating the fundamental interactions and geometrical features to the macroscale stress-strain behavior in non-woven and non-bonded mats is still lacking.

In this work, we perform a detailed study of the effect of fiber crimp and contact properties (adhesion and friction) on the mechanics of non-crosslinked fibrous mats stabilized by adhesion. We show that the mechanics of nanofibrous mats of

this type is dominated by frictional energy dissipation. The relationship between the yield stress and post-yield strain hardening, and the geometric and adhesion/friction parameters of the system is defined. Networks with infinite and finite length fibers are studied, and it is observed that their mechanics is identical, except at large strains, when networks of infinite fibers strain stiffen, while those of finite length fibers become unstable. Given the prevalence of such fibrous materials in many soft materials, both biological and artificial materials, we expect that the present results will prove useful in the design and general system evaluation.

2. Models and methodology

2.1 Network generation

We consider linear elastic athermal fibers of elastic modulus E, fiber diameter d, and contour length L_f . The fiber diameter d is used here as the unit of length and Ed^2 is considered the unit of force. Fibers form a quasi-2D network in the form of a mat, such as that shown in Fig. 1(a). The structure is three-dimensional, as fibers are not allowed to cross. The plane of the mat is X-Y and the mat thickness is measured in the Z direction.

Fibers are allowed to be wavy in their undeformed state and the degree of waviness is characterized by the persistence length, $L_{\rm P}$. The directional auto-correlation of the fiber tangent vector can be characterized by computing $\cos\theta'(l)$, where $\theta'(l)$ is the angle between the tangent versors at two points along a given fiber separated by the contour length l, and an overbar indicates averaging over multiple fibers and reference points. The directional auto-correlation function is approximated as

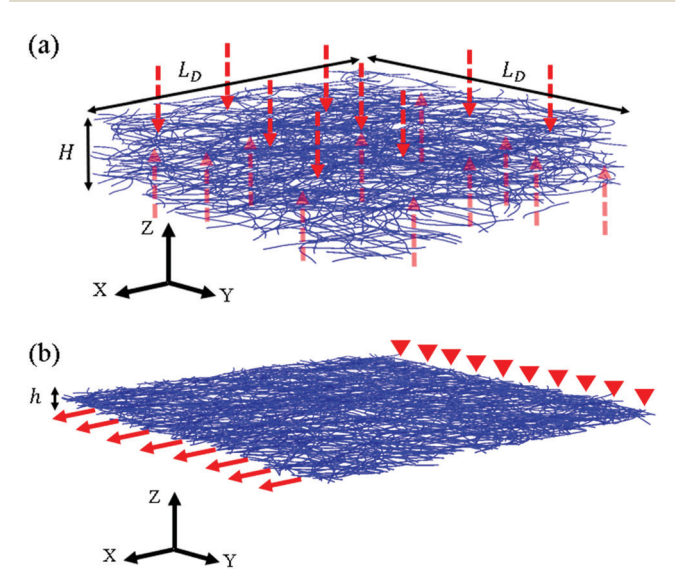


Fig. 1 (a) Representation of a quasi-2D network of wavy fibers. The red dashed arrows show the compaction force used in the network generation step. $L_{\rm D}$ and H are the model in-plane and thickness dimensions. (b) A realization of a compacted, adhesion stabilized quasi-2D fiber network resulting from (a). The mat thickness after compaction is h. The figure also shows a schematic of the boundary conditions applied when probing the mechanical behavior of the mat.

 $\cos \theta'(l) \approx \exp(-l/L_{\rm P})$, from where the persistence length parameter, $L_{\rm P}$, is obtained. This parameter characterizes the magnitude of fiber waviness.

Although, in general, fibers may show waviness in 3D, we allow fibers to be wavy only in the *X-Y* plane, which is adequate for mats produced by additive processes such as electrospinning.

Each fiber is created as a series of coplanar equal-sized rectilinear segments of length l_s . We use angularly restricted correlated random walk in 2D to generate the wavy fibers. To this end, we choose a starting point p_0 and a starting direction n_0 for the random walk, which is then generated with step length l_s . The angular deviation between consecutive steps iand i + 1, i.e. $\cos^{-1}(n_i \cdot n_{i+1})$, where n_i , which denotes the direction of the walk at step i, is sampled from a Uniform Distribution in the interval $(-\alpha, \alpha)$. Similar models have been used to characterize and represent planar fibrous biomaterials. 4,19 For this procedure, $L_{\rm P}$ is related to α as $L_{\rm P}/l_{\rm s} = 6/\alpha^2$, which is accurate for small values of α , as discussed in the Appendix. Furthermore, the root mean-square end to end distance of the fiber is $r_{\rm rms}=\sqrt{\langle r^2 \rangle}=L_{\rm P}\sqrt{2(\exp(-L_{\rm f}/L_{\rm P})-1+L_{\rm f}/L_{\rm P})}.^{41}$ An alternate, equivalent measure of crimp used in the literature is the relative fiber slack represented by $L_{\rm f}/r_{\rm rms}-1,^{42}$ or alternateivly as $\langle L_{\rm f}/r \rangle - 1.^{5,30,40}$

Fibers are generated in a box of size $L_D \times L_D \times H$ and parallel to the X-Y plane, Fig. 1(a). Each such planar fiber is given a random offset in the Z direction between -H/2 and +H/2. We study two types of networks with 'infinite' fibers (which percolate across the simulation domain), and with fibers of finite length. To generate an infinite fiber, we randomly chose a point on one of the four side boundaries and a random inward pointing direction to initiate the random walk. In the finite length fiber case, we follow the Mikado network generation process. ^{43,44} We randomly select a point p_0 inside the X-Y plane and a random direction n_0 . Assuming p_0 to be the mid-point of a wavy fiber, we start two random walks of length $L_f/2$ in the n_0 and $-n_0$ directions. A walk always stops at the domain boundary. In order to limit size effects in the computed effective properties of the network, the characteristic lengths of fibers, L_P and L_f (in the infinite and finite length cases, respectively), are taken 2 to 3 times smaller than the model size, L_D .

This process creates an aperiodic assembly of planar wavy fibers. The actual structure of the quasi-2D network is obtained by applying a temporary compacting (body) force-field in the Z direction, as shown by the dashed arrows in Fig. 1(a). The compaction process is simulated with inter-fiber interactions such as excluded volume, friction, and adhesion activated (Section 2.2). This enables adhesion to stabilize the network. The body force is removed after the compaction process.

2.2 Inter-fiber interactions

The types of interactions between fibers considered here are of non-bonded type: excluded volume, adhesion, and friction. Unlike bonded type interactions such as permanent crosslinks, which act at pre-determined sites, non-bonded interactions act only at inter-fiber contacts during the duration of the contact.

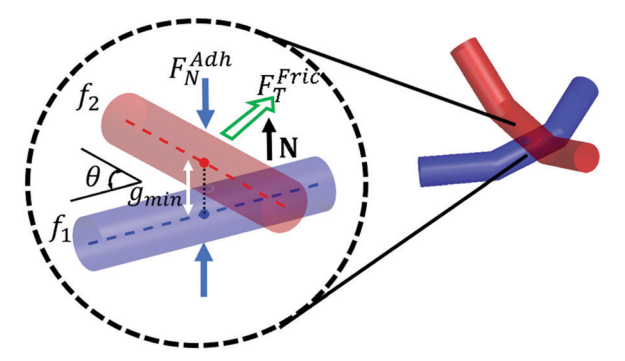


Fig. 2 Schematic representation of a point contact between two fibers. Note that the contact normal **N** shown in the figure is with respect to fiber f_2 . The contact normal for fiber f_1 is $-\mathbf{N}$.

Contacts can be of line or point type. The line contacts prevail in networks in which fibers bundle. Such structures were studied by Negi and Picu³⁵ and Sengab and Picu,³⁶ where it is shown that adhesion-driven self-organization is prevented once inter-fiber friction is accounted for. Point contacts prevail in the presence of friction and adhesion. This motivates the exclusive consideration of point contacts in this work.

Fig. 2 shows a schematic of a point contact between two fibers, f_1 and f_2 . A point contact is established when the minimum separation distance, g_{\min} , between the centerlines of two fibers becomes less than d. The local normal direction of the contact, N, is defined by the cross-product of the tangent versors to the two fibers at the contact point. It is noted that N is a unit vector (versor).

The excluded volume interaction, $F_{\mathbf{N}}^{\mathrm{EV}} = K_{\mathbf{p}} \langle d - g_{\min} \rangle \mathbf{N}$, where $\langle \rangle$ is the Macaulay bracket, leads to a repulsive force acting on the fibers forming the contact in the direction of \mathbf{N} of each of the fibers in contact. $K_{\mathbf{p}}$ is a constant penalty stiffness for interfiber penetration which ensures numerical convergence and accuracy of the simulation procedure. ³⁰

In this work, we implement adhesion by applying a normal attractive force of magnitude $F_{\rm N}^{\rm Adh}$ at each established contact, when $d-g_{\min}>0$, in addition to the excluded volume interaction. Hence, the net normal contact force is F_N = $[K_p\langle d-g_{\min}\rangle-F_N^{Adh}H(d-g_{\min})]N$, where H() is the unit step function. This renders the equilibrium $d-g_{\min}$ slightly negative at all contacts in the absence of any external load. In general, adhesion at a contact point is specified using a force-separation relationship between the normal force at a contact F_N and contact-penetration ($d-g_{min}$). Various force-separation relationships are proposed in the literature for different strengths of adhesion and stiffness of contacting fibers, such as the Derjaguin-Muller-Toporov (DMT)⁴⁵ and the Johnson-Kendall-Roberts (JKR)⁴⁶ models. Experimental studies show that contacts between polymeric fibers follow the JKR model. 47,48 In the present simulations we do not represent explicitly the dynamics of contact opening and closing on time scales defined by the local elasticity at each individual fiber contact. Instead, we use a threshold condition defined in terms of the separation force: the contact opens when the force is larger than a critical value. We observe (Section 3.3) that very few contacts (less than 5%) open during deformation up to 5% strain.

The tangential force required for sliding of contacts between fibers is denoted as $F_{\rm T}^{\rm Fric}$. This frictional force can be either of the Coulomb type, *i.e.* proportional to the normal external load applied to the contact, or proportional to the contact area. In the case of nanofibers, it is more likely that this force is of the second type. This case is described by Bowden and Tabor⁴⁹ theory of adhesive friction where $F_{\rm T}^{\rm Fric} = A\tau_0$, with A being the contact area and τ_0 the 'frictional shear stress'. τ_0 is considered constant for given contacting surfaces in a given environment. Experimental studies of Homola $et\ al.^{50}$ and Carpick $et\ al.^{51}$ provide support to this description. In the present models, we adopt this physical view. The contact is considered circular in most models. In Section 3.5, we discuss the more realistic case in which the contact area is allowed to be non-circular and dependent on the angle θ between fibers.

Therefore, the inter-fiber point contact is defined by two parameters, F_N^{Adh} and F_T^{Fric} . These forces can be non-dimensionalized using Ed^2 , which gives the non-dimensional force parameters $\Psi_N^{\text{Adh}} = F_N^{\text{Adh}}/Ed^2$ and $\Psi_T^{\text{Fric}} = F_T^{\text{Fric}}/Ed^2$.

2.3 Numerical modeling

The fibers are meshed using two-node Timoshenko 3D beam elements with element size $l_{\rm e}$ equal to the segment size $l_{\rm s}$ of the geometrical discretization described in Section 2.1. The aspect ratio of the elements, $l_{\rm e}/d$, is taken to be 5 for computational efficiency.

The model is solved using the commercial Finite Element package ABAQUS (2017). Excluded volume interactions are represented using the penalty stiffness model of beam-to-beam contact in ABAQUS. Attractive adhesive force F_N^{Adh} is applied at each contact during the simulation using a user-defined FORTRAN subroutine. In this subroutine, the nodal displacements/positions are extracted at every solution increment by defining them as 'sensor-output' data in ABAQUS. Furthermore, at each solution increment the contacting elements are determined from the nodal positions using a global contact detection algorithm inspired by the Cell Linked-List (CLL) algorithm in molecular dynamics.⁵² Specifically, a fixed simulation box is created encompassing the elements. This simulation box is divided into cubic cells with edge length larger than, or equal, to l_e . The elements are associated with their respective cells based on their centroid position and stored as a linked-list data structure. The detection of contacting elements for each element involves searching over its own cell's elements as well as elements in the neighboring 26 (in 3D) cells. This algorithm offers an advantage of having O(n) time complexity, with n being the number of elements in the simulation.

 $E_{\mathrm{T}}^{\mathrm{Fric}}$ is defined by using the VFRICTION subroutine in ABAQUS. Furthermore, contact damping is also applied for numerical stability. The simulations are carried out using the explicit time integration scheme at sufficiently low loading rates to represent quasi-static conditions.

2.4 Solution procedure

After the initial fiber layout process described in Section 2.1, the network is compacted by applying a temporary body (line)

force on fibers in the *Z*-direction, F_Z , such that $F_Z = -P_0 \varsigma(t) z$, where P_0 is proportional to the maximum magnitude of the force and $\varsigma(t)$ describes the variation of the force-field with time. $\varsigma(t)$ smoothly increases from 0 to 1 and returns to 0 during the compaction process. This procedure enables the formation of contacts which remain stable even after the removal of F_Z due to the adhesive forces. The value of P_0 is selected as the minimum value above which the number of contacts at the end of mat compaction is independent of this parameter. A realization of the compacted quasi-2D network is shown in Fig. 1(b).

Similar approaches of fiber deposition have been used in the literature. ^{19,21,22,30} The compaction force is taken to be either a model parameter or equal to the gravitational force. ^{19,21} In these cases, the compaction force is permanent and determines the final structure of the mat, *i.e.* the density of contacts, the mat porosity, *etc.* Liu and Dzenis²² compacted the network by forcing the ends of long fibers to belong to a common plane. Kulachenko and Uesaka³⁰ successively deposited straight, flexible fibers such that every newly deposited fiber bends at contacts and conforms to the underlying fibers up to the level where the slope of the resulting fiber undulations in the direction perpendicular to the mat plane does not exceed 30°.

To probe the mechanics of these networks, the mats (Fig. 1(b)) are loaded in uniaxial tension by imposing displacements along the two model boundaries perpendicular to the X direction. Traction free conditions are applied along the model boundaries perpendicular to the Y and Z directions. We report the work conjugate second Piola–Kirchhoff stress Π_{xx} and the Green–Lagrange strain ε_{xx} . Π_{xx} is computed as the force per unit length of the boundary and is non-dimensionalized as $\hat{\Pi} = \Pi/Ed$.

3. Results

3.1 System parameters

In order to develop a broad physical picture of the structureproperty relation for these networks, the system parameters described above, Ψ_{N}^{Adh} , Ψ_{T}^{Fric} , and L_{P} , are varied in a range relevant for applications. Ψ_{N}^{Adh} and Ψ_{T}^{Fric} vary in the range of 2.5×10^{-6} – 2.5×10^{-4} . For a polymeric fiber of elastic modulus E, diameter d, and surface energy (J m⁻²) γ , Ψ_N^{Adh} of a point contact between two perpendicular fibers calculated as per JKR theory⁴⁶ is $1.5\pi\gamma/Ed$. For a polyacrylonitrile (PAN) nanofiber with surface energy $\gamma \sim 0.050~\mathrm{J~m}^{-253}$ and $E \sim 3~\mathrm{GPa}$, $\Psi_\mathrm{N}^\mathrm{Adh}$ is $\sim 2.62 \times 10^{-4}$ for d = 300 nm and $\sim 2.62 \times 10^{-6}$ for d = 30 μ m. Likewise, for polystyrene (PS) with $E \sim 3$ GPa, $\gamma \sim 0.041$ J m⁻²,⁵³ and d = 300 nm and 30 μ m $\Psi_{\rm N}^{\rm Adh} \sim 2.15 \times 10^{-4}$ and $\sim 2.15 \times$ 10⁻⁶ respectively. These values are typical for various polymeric nanofibers. $\Psi_{\rm T}^{\rm Fric}$ is also taken to be in the same range as $\Psi_{\rm N}^{\rm Adh}$. While, γ and E may not vary significantly from one polymeric material to another, it is by adjusting the fiber diameter, d, that $\Psi_{\rm N}^{\rm Adh}$ and $\Psi_{\rm T}^{\rm Fric}$ acquire a broad range of variation. $L_{\rm P}$ is taken to be ∞ , 500d, 250d, 167d, and 100d in separate simulations. The network density, denoted by ρ , is measured as the total fiber length per unit projected area of the mat in the X-Y plane. ρd is

Table 1 Parameters of networks considered in this work. $L_{\rm f}/d=\infty$ indicates 'infinite' fibers and $L_{\rm P}/d=\infty$ indicates straight fibers. ρd is the nondimensional density. τ is the tortuosity, defined as $\tau=\overline{L_{\rm f}/r}-1$, where r is the end-to-end distance of a fiber and the overbar indicates averaging over the entire fiber set

Case no.	$L_{ m P}/d$	$L_{ m f}/d$	$\Psi_{ m N}^{ m Adh}$	$\Psi_{ m N}^{ m Fric}$	ρd	τ
I	∞	∞	Various	$\Psi_{ m N}^{ m Adh}/10$	0.96	0
II	∞	∞	Various	$\Psi_{ m N}^{ m Adh}/10$	1.92	0
III	250	∞	Various	Various	0.48	1.24
IV	100	∞	2.5×10^{-5}	2.5×10^{-5}	0.48	2.91
V	167	∞	2.5×10^{-5}	2.5×10^{-5}	0.48	1.85
VI	500	∞	2.5×10^{-5}	2.5×10^{-5}	0.48	0.39
VII	250	250	2.5×10^{-4}	2.5×10^{-5}	0.48	0.15
VIII	∞	250	2.5×10^{-4}	Various	0.48	0

the nondimensional network density, which is taken here to be in the range of 0.48 to 1.92.

Table 1 presents specific cases considered in this work. Three realizations are considered for each of these cases and the average response of these realizations is presented. Cases I and II represent networks of straight infinite fibers of two densities, $\rho d = 0.96$ and 1.92 respectively. Cases III to VI represent networks of infinite wavy fibers of the same density but increasing persistence length, $L_{\rm P}$. Cases VII and VIII correspond to networks of finite length fibers which are wavy and straight, respectively, but having the same network density.

Fig. 3(a) shows the parametric space of these systems. The space is defined by the fiber material property Ed^2 , the geometric parameter, $L_{\rm P}$, and the contact properties $F_{\rm N}^{\rm Adh}$ and $F_{\rm T}^{\rm Fric}$. The figure highlights the region of the parametric space considered in this work. The region where $\Psi_{\rm N}^{\rm Adh}$ and $\Psi_{\rm T}^{\rm Fric} \ll 2.5 \times 10^{-6}$ (the slopes indicated in Fig. 3(a) and (b) represent Ψ_{N}^{Adh} and $\hat{\Psi_{T}^{Fric}}$ corresponds to the trivial case of negligible inter-fiber interactions, in which the response of the mat is simply the average of the response of individual wavy fibers loaded by the far field (no fiber-fiber interactions and "infinite" fibers). When $\Psi_{
m N}^{
m Adh}$ and $\Psi_{\rm T}^{\rm Fric} \gg 2.5 \times 10^{-4}$, adhesion is strong and it is expected that it drives fiber alignment and bundling leading to non-crosslinked networks such as those discussed in ref. 34. Furthermore, straight fibers $(L_P \to \infty)$ running across the problem domain are too stiff to be affected by contact forces. In such networks, the mechanics is governed largely by the constitutive behavior of the fibers. 22 Likewise, the regime of very small L_P is not realistic. Therefore, the scope of this work is limited to the shaded range in Fig. 3. Fig. 3(b) shows a projection of the parametric space in Fig. 3(a) along with the locus corresponding to a broad range of polymeric mats of nano- and micro-fibers. Most of this locus is covered by the range of parameters considered here (shaded region).

3.2 Structure of fiber mats

The structure of the mats is characterized by the mean fiber contour length between contacts, $l_{\rm c}$, and the mat thickness, h. These result from the collective organization of the fibers for a given set of network parameters ρ , d, and $\Psi_{\rm N}^{\rm Adh}$. The objective of this section is to define this relationship.

Parameter l_c depends on the degree of mat compaction under the action of adhesion and hence is controlled by Ψ_N^{Adh} . Note that

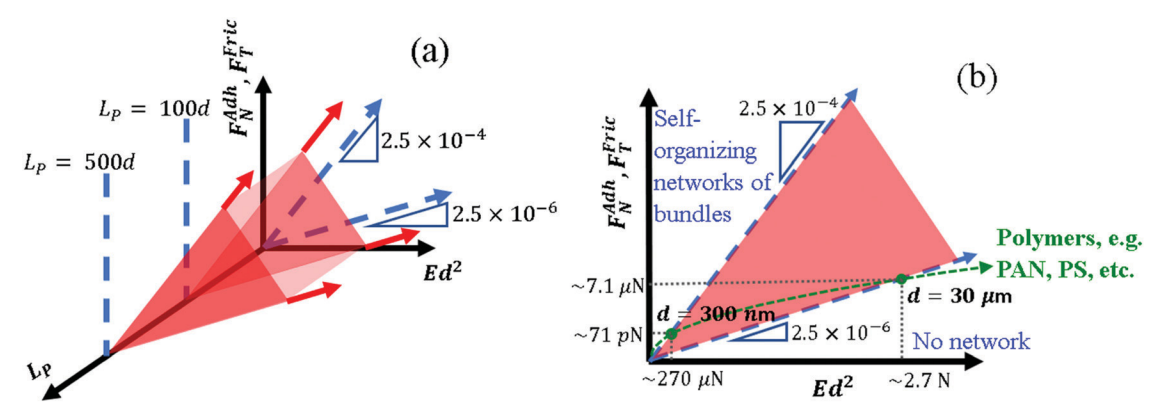


Fig. 3 (a) Parametric space of the present problem, with the region considered in this study shaded (in red). (b) Projection of the space shown in (a) showing regimes discussed in the text and the locus corresponding to polymeric nano and microfiber mats (curved dashed arrow). The slopes indicated in (a) and (b) represent Ψ_N^{Adh} and Ψ_T^{Fric} .

 l_c is significantly larger than the Kallmes–Corte⁵⁴ prediction for a set of straight lines placed at random on a plane (2D Mikado network), $\pi/2\rho$, because in the 3D structure fibers do not make contacts at all points at which they cross in the *X–Y* projection. Similarly, the thickness of the mat, h, is also an outcome of the model. h is evaluated as twice the standard deviation of the mass distribution in the Z direction after compaction (Fig. 1(a)).

Fig. 4(a) shows the relation between $l_{\rm c}$ and $\Psi_{\rm N}^{\rm Adh}$. The curves correspond to three densities (Table 1). It is seen that ρ and $L_{\rm P}$ have essentially no effect on $l_{\rm c}$, while a power law is established between $l_{\rm c}$ and $\Psi_{\rm N}^{\rm Adh}$:

$$l_c \sim \psi_{\rm N}^{\rm Adh^{-0.29}} \tag{1}$$

This indicates that, as opposed to the purely geometric analysis leading to the Kallmes–Corte relation where $l_{\rm c}$ is an extensive quantity related to ρ , the segment length $l_{\rm c}$ in this problem is defined by mechanics and it is intensive in nature, *i.e.* independent of ρ .

Fig. 4(b) shows that $l_{\rm c}$ is proportional to h. As ρ increases, the network thickness increases at a constant internal structure and $l_{\rm c}$, Fig. 4(a). Therefore, the thickness of the networks h

must be proportional to ρ . We report $h/\rho d^2$ as a normalized (intensive) measure of height. The overlap of the $h/\rho d^2$ vs. l_c/d curves for networks of various ρ in Fig. 4(b) confirms the intensive nature of this parameter. Combining the results in Fig. 4(a) and (b), it is observed that $h \sim \rho d^2 \Psi_N^{\text{Adh}-0.29}$. Note that, as stated above, all these results correspond to the state of the mat after removing the compaction force.

Since the effective volume of the mat is $hL_{\rm D}^{\ 2}$ and $L_{\rm D}$ is essentially independent of $\Psi_{\rm N}^{\rm Adh}$, the proportionality relation in Fig. 4(b) implies:

$$l_{\rm c} \propto \frac{hdL_{\rm D}^2}{\rho d^2 L_{\rm D}^2} \propto \frac{d}{\phi}$$
 (2)

where ϕ is the volume fraction of fibers in the network.

Forced packing of slender fibers under compression without inter-fiber adhesion or friction was studied analytically in ref. 24 and 25 for 3D networks, and in ref. 23 for quasi 2D networks. A general expression derived for $l_{\rm c}$ in ref. 25 and 55 is $l_{\rm c}=\pi d/8f$, where f depends on fiber orientation (f is $\pi/4$ and $2/\pi$ for 3D and 2D random orientations respectively). Eqn (2) is in agreement with this analytical result.

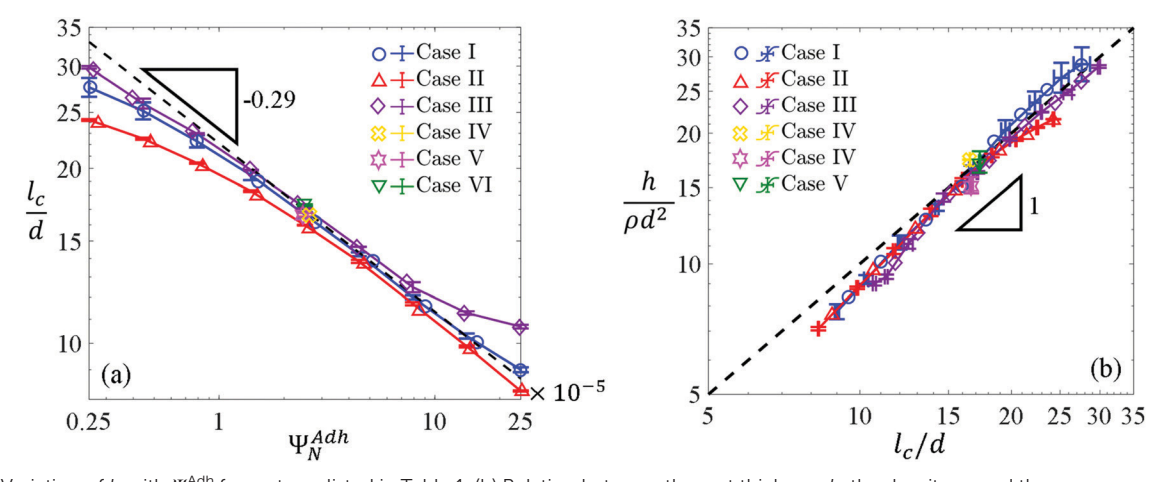


Fig. 4 (a) Variation of l_c with Ψ_N^{Adh} for systems listed in Table 1. (b) Relation between the mat thickness h, the density, ρ , and the mean segment contour length l_c . The bars represent the standard error of 3 realizations.

These analyses also indicate that the pressure required to compact the network to achieve fiber volume fraction is $p \propto EI(\phi^n-\phi_0^n)$, where ϕ_0 is the volume fraction of the as-deposited packing, and n is 3 and 5 for $3D^{24}$ and $2D^{23}$ networks respectively. The networks considered in the present work are held together by the inter-fiber adhesion, with no external pressure being applied. To understand the scaling relations in Fig. 4 in the context of previous results on pressure-driven compaction, we consider that the adhesion forces act as an equivalent pressure of magnitude:

$$p_{\rm eff} \sim \rho \frac{F_{\rm N}^{\rm Adh}}{l_{\rm c}} \tag{3}$$

Using $p_{\rm eff}$ in the pressure-density relation for quasi-2D mats, $p \propto EI(\phi^5 - \phi_0^5)$, ²³ and assuming $\phi_0 \ll \phi$, it is found that:

$$p_{\rm eff} \sim \rho \frac{F_{\rm N}^{\rm Adh}}{l_{\rm c}} \sim EI\phi^5 \sim EI\left(\frac{d}{l_{\rm c}}\right)^5$$
 (4)

which implies that

$$F_{\rm N}^{\rm Adh} \propto l_{\rm c}^{-4}$$
 (5)

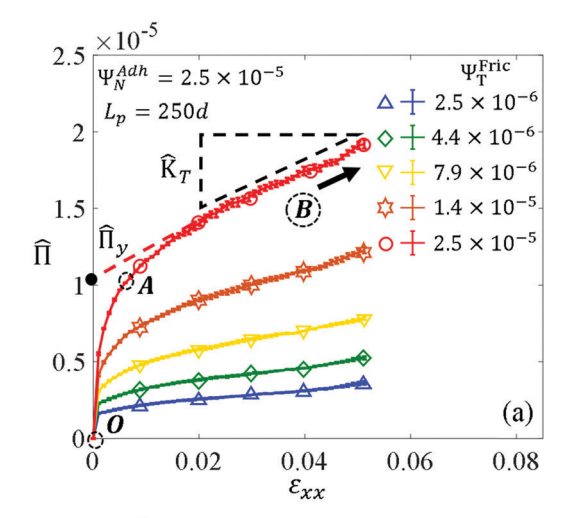
Eqn (5) implies that $l_{\rm c} \sim \Psi_{\rm N}^{\rm Adh-0.25}$ which is in good agreement with the results in Fig. 4(a) and eqn (1).

The deviation from the power-law scaling for $\Psi_{\rm N}^{\rm Adh} < 2.5 \times 10^{-6}$ seen in Fig. 4(a) is attributed to the size-effect which comes into play when $l_{\rm c}$ approaches the simulation domain size $L_{\rm D}$. On the other hand, the deviation observed when $\Psi_{\rm N}^{\rm Adh} > 2.5 \times 10^{-4}$ is a result of $l_{\rm c}$ approaching the 2D lower bound predicted by the Kallmes–Corte relations $(\pi/2\rho)$, a situation in which the present concepts do not apply. This is supported by the observation that the deviation increases with decreasing ρ (compare case III $(\rho d = 0.48)$ with cases I $(\rho d = 0.96)$ and II $(\rho d = 1.92)$).

3.3 Tensile response of mats with infinite wavy fibers

In this section we discuss the dependence of the tensile response of the mats of infinite wavy fibers on system parameters describing friction and adhesion, $\Psi_{\rm T}^{\rm Fric}$ and $\Psi_{\rm N}^{\rm Adh}$, and on fiber tortuosity, $L_{\rm P}$. Fig. 5(a) shows stress-strain curves obtained with mats belonging to case III (Table 1), having the same $\Psi_{\rm N}^{\rm Adh}$ ($\Psi_{\rm N}^{\rm Adh}$ = 2.5 × 10⁻⁵) and $L_{\rm P} (L_{\rm P} = 250 d)$, and different $\Psi_{\rm T}^{\rm Fric}$. The curves exhibit two regimes. The first regime (OA) is linear elastic and is observed at very small strains. In this regime, the contacts are not loaded enough for sliding to occur, and hence they behave similar to permanent bonds. Once the tangential load exceeds $\Psi_{\mathrm{T}}^{\mathrm{Fric}}$ at some contacts, slippage begins. In regime II, (AB) a moving phase percolating across the model forms, thereby producing global plastic flow. The curves are described by two parameters: the effective yield stress, $\hat{\Pi}_{v}$, and the strain hardening modulus observed in regime II, \hat{K}_T . The yield stress is defined conventionally as the intercept of the tangent to the regime II branch of the curve with the vertical axis.

Fig. 5(b) shows the stress–strain response of cases III, IV, V, and VI, *i.e.* networks with $\Psi_{\rm N}^{\rm Adh} = \Psi_{\rm T}^{\rm Fric} = 2.5 \times 10^{-5}$ and various $L_{\rm P}$. These curves exhibit the two regimes described above, and a



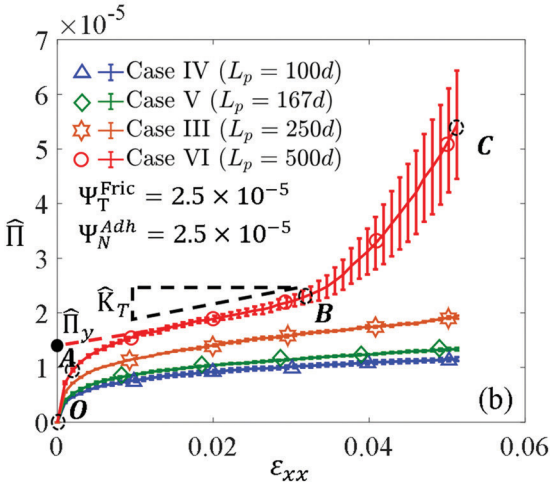


Fig. 5 Stress–strain curves for networks with (a) different $\Psi_{\rm T}^{\rm Fric}$ and the same $L_{\rm P}$, and (b) different $L_{\rm P}$ and the same $\Psi_{\rm T}^{\rm Fric}$. $\Psi_{\rm N}^{\rm Adh}=2.5\times10^{-5}$ in all cases. The bars represent the standard error of the 3 realizations.

third regime of rapid strain stiffening at larger strains (BC in Fig. 5(b)). This regime is observed only in the case of infinite fibers when some of the wavy fibers straighten out and are loaded axially forming stress-paths. This phenomenon is also observed in cross-linked networks subjected to tension at large strains. 42,56 The onset of regime III depends on L_P and moves to larger strains as L_P decreases.

In order to understand the behavior shown in Fig. 5, it is useful to discuss the nature of stress in these networks. We show here that mechanics is associated with frictional dissipation at contacts, which contrasts with the usual situation in cross-linked networks, where stress is associated with the variation of the strain energy during deformation.

To this end, consider a fiber of the mat, having elastic modulus E, diameter d, bending stiffness EI, persistence length $L_{\rm P}$, contour length $L_{\rm f}$, and end-to-end distance r. The effective small-strain stiffness of the wavy fiber measured by stretching in the direction of the end-to-end vector can be estimated as $45L_{\rm P}EI/L_{\rm f}^4$. If a small strain ε is applied, the strain energy is $(45L_{\rm P}EI/L_{\rm f}^4)r^2\varepsilon^2/2$. On the other hand, energy is dissipated at

sliding contacts with other fibers. Assuming affine deformation of the fiber, the expected frictional work performed during sliding is estimated to be approximately $F_T^{\text{Fric}} re L_f / 2l_c$. The mechanics is dominated by frictional dissipation if $F_{\rm T}^{\rm Fric} re L_{\rm f}/2l_{\rm c} \gg (45 L_{\rm p} EI/$ $(L_{\rm f}^4)r^2\varepsilon^2/2$. This simplifies to $\Psi_{\rm T}^{\rm Fric}>2.2\varepsilon(l_{\rm c}L_{\rm F}rd^2/L_{\rm f}^5)$. For parameters such as those considered here (specifically, $l_{\rm c}$ = 15d, $r \approx L_{\rm f} \approx$ $L_{\rm D}$ = 500d, ε = 0.05, and $L_{\rm P}$ = 250d) this inequality can be written as $\Psi_{\rm T}^{\rm Fric} > 6.5 \times 10^{-9}$. Since $\Psi_{\rm T}^{\rm Fric} \in (2.5 \times 10^{-6}, 2.5 \times 10^{-5})$ in the current models, mechanics is dissipation-dominated (nonconservative) rather than strain energy-dominated (conservative). This is also observed by directly comparing the strain energy variation during deformation, which is the energetic component of stress, with the work performed by the tractions applied at the boundary of the model. The strain energy represents only $\sim 15\%$ of the total work, which supports the conclusion that the mechanics in these systems is associated with frictional dissipation.

With this understanding of the origin of stress, we discuss now the kinematics. To this end, we consider case III networks whose stress-strain curves are shown in Fig. 5(a). These have the same $L_{\rm P}$ and different $\Psi_{\rm T}^{\rm Fric}$. Three parameters are monitored: the total number of contacts, N_c , the number of actively sliding contacts in each strain increment, $N_{\rm a}$, and the rate of slip in the active contacts. The mean rate of slip is defined as $\bar{s} = \langle ds/d\varepsilon_{xx} \rangle$, where s is the magnitude of slip occurring at a contact, $ds/d\epsilon_{xx}$ is the rate of slip at given contact versus the applied far-field strain, and the angular bracket indicates averaging over all contacts in the model. The variation with the strain of these three parameters is shown in Fig. 6. Fig. 6(a) shows N_c and N_a normalized by the total number of contacts in the initial configuration, at zero strain, N_0 . The total number of contacts remains constant during deformation, up to the maximum strain applied (5%). The number of actively sliding contacts, N_a , increases fast during regime I of the stress-strain curve and remains constant in regime II. N_a decreases with increasing $\Psi_{\rm T}^{\rm Fric}$. The mean slip rate at contacts, \bar{s} , increases continuously with strain in regime II and is essentially independent of $\Psi_{\rm T}^{\rm Fric}$, Fig. 6(b).

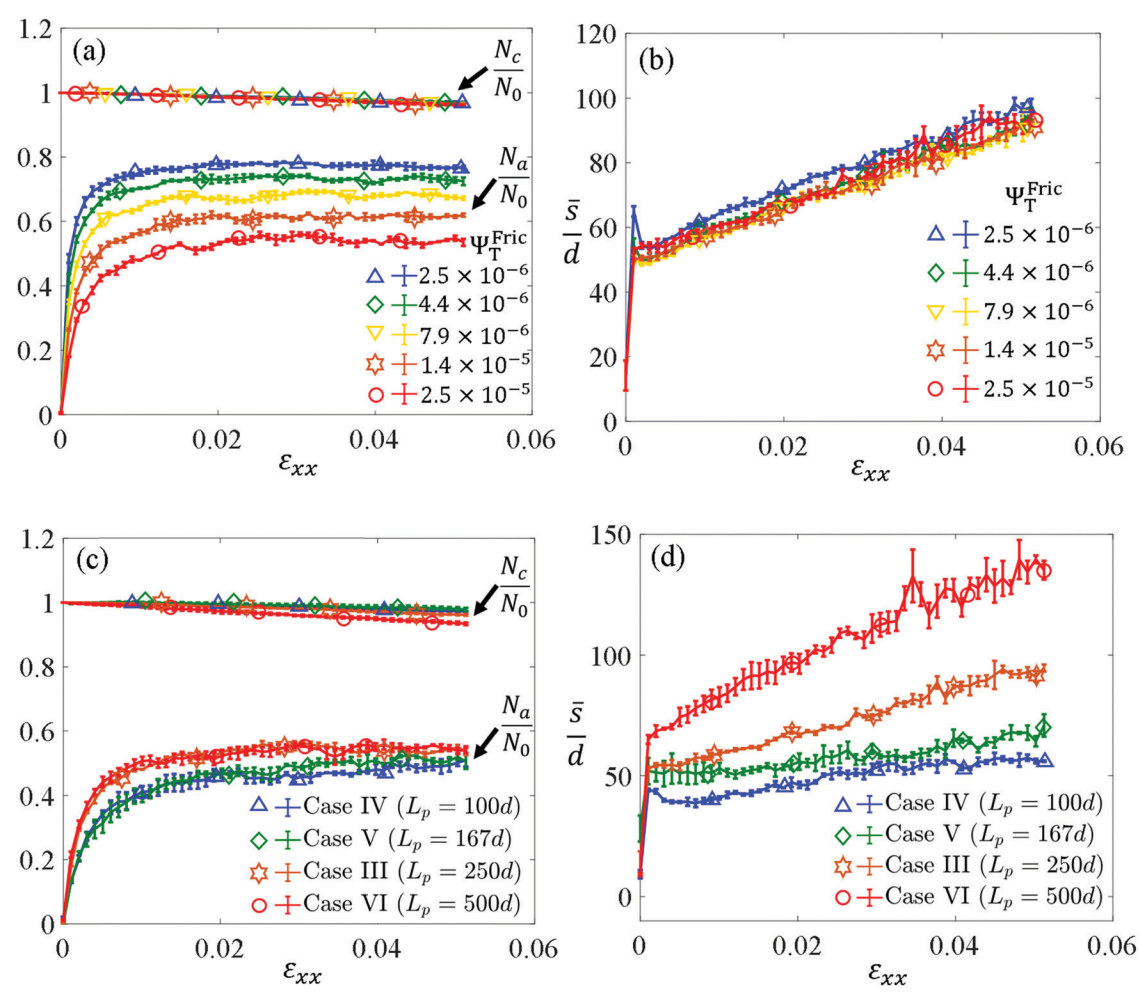


Fig. 6 Variation during deformation of ((a) and (c)) the total number of contacts, N_c , and of the number of actively sliding contacts, N_a , and of ((b) and (d)) the mean slip rate at actively sliding contacts, $\bar{s} = \langle \text{ds}/\text{d}\varepsilon_{xx} \rangle$. N_c and N_a are normalized by the total number of contacts in the strain-free state, N_0 . (a) and (b) correspond to mats of different Ψ_T^{Fric} and same $L_P = 250d$ (case III in Table 1), while (c) and (d) correspond to mats of different L_P and same $\Psi_T^{\text{Fric}} = 2.5 \times 10^{-5}$ (cases III to VI in Table 1). The stress–strain curves for these networks are shown in Fig. 5(a) and (b), respectively. The bars indicate the standard error of three realizations.

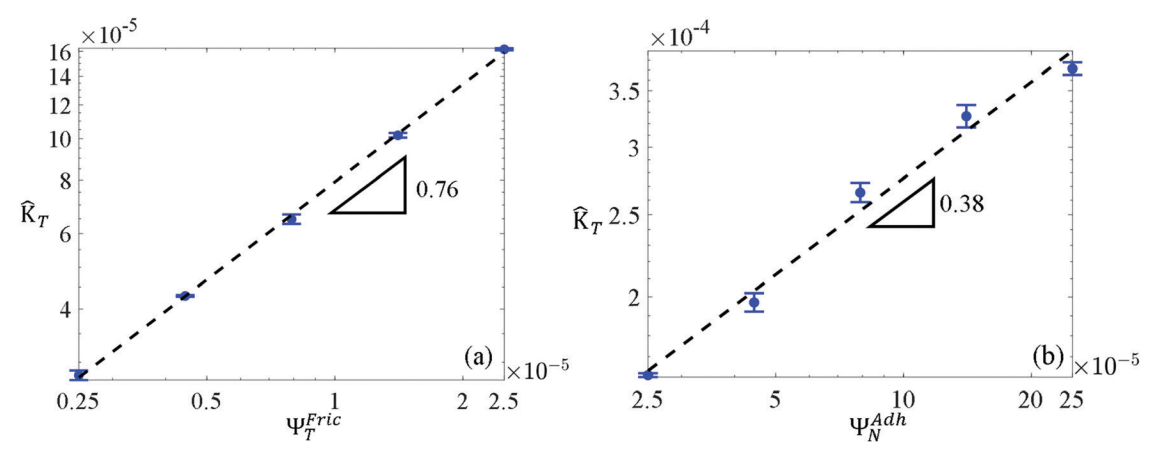


Fig. 7 Dependence of regime II strain hardening, \hat{K}_T , on (a) Ψ_T^{Fric} (with $\Psi_N^{Adh} = 2.5 \times 10^{-5}$) and (b) Ψ_N^{Adh} (with $\Psi_T^{Fric} = 2.5 \times 10^{-5}$).

Considering that the external work performed by the applied stress corresponds to frictional dissipation at contacts, one may write:

$$\hat{\Pi} \sim \mathrm{d}W_{\mathrm{fric}}/\mathrm{d}\varepsilon_{xx} \sim \Psi_{\mathrm{T}}^{\mathrm{Fric}}N_{\mathrm{a}}\bar{s}$$
 (6)

Eqn (6) also indicates the dependence of \hat{K}_T on Ψ_T^{Fric} , N_a and \bar{s} :

$$\hat{K}_{T} \sim d(\Psi_{T}^{Fric} N_{a} \bar{s})/d\varepsilon_{xx} = \Psi_{T}^{Fric} N_{a} d\bar{s}/d\varepsilon_{xx}$$
 (7)

Hence, for each of the stress–strain curves in Fig. 5(a) (given $\Psi_{\rm T}^{\rm Fric}$), the strain hardening modulus $\hat{K}_{\rm T}$ should be non-zero since \bar{s} increases continuously with strain, Fig. 6(b). This traces the origin of the regime II strain hardening to the gradual increase of the sliding distance per increment of the applied far-field strain observed in Fig. 6(b).

Since $d\bar{s}/d\varepsilon_{xx}$ is independent of $\Psi_{\rm T}^{\rm Fric}$ and $N_{\rm a}$ decreases with increasing $\Psi_{\rm T}^{\rm Fric}$, $\hat{K}_{\rm T}$ should increase sub-linearly with $\Psi_{\rm T}^{\rm Fric}$. Fig. 7(a) shows the variation of $\hat{K}_{\rm T}$ with $\Psi_{\rm T}^{\rm Fric}$ determined from the curves in Fig. 5(a). It is seen that

$$\hat{K}_{\rm T} \sim \Psi_{\rm T}^{\rm Fric3/4}$$
 (8)

Fig. 7(b) shows the variation of \hat{K}_T with Ψ_N^{Adh} obtained with case III type models having the same Ψ_T^{Fric} . Again, we observe a power-law relation:

$$\hat{K}_{\rm T} \sim \Psi_{\rm N}^{\rm Adh0.38} \tag{9}$$

Eqn (1) indicates that Ψ_N^{Adh} changes the structure of the network. The number of contacts, N_c , is inversely proportional to l_c (at given L_p), and using eqn (7) one infers that $\hat{K}_T \sim N_a \sim N_c \sim l_c^{-1} \sim \Psi_N^{\text{Adho.29}}$. This is in reasonable agreement with the exponent in eqn (9), which provides support for the physical interpretation proposed here.

The dependence of the yield stress \hat{H}_y on system parameters can also be understood based on eqn (6) and the data in Fig. 6(a) and (b). At yield, \bar{s} is independent of $\Psi_{\rm T}^{\rm Fric}$, while $N_{\rm a}$ decreases with increasing $\Psi_{\rm T}^{\rm Fric}$. Therefore, \hat{H}_y increases sublinearly with $\Psi_{\rm T}^{\rm Fric}$, as can be seen in Fig. 5(a). More precisely, $\hat{H}_y \sim \Psi_{\rm T}^{\rm Fric^{3/4}}$ which is a relation similar to eqn (8).

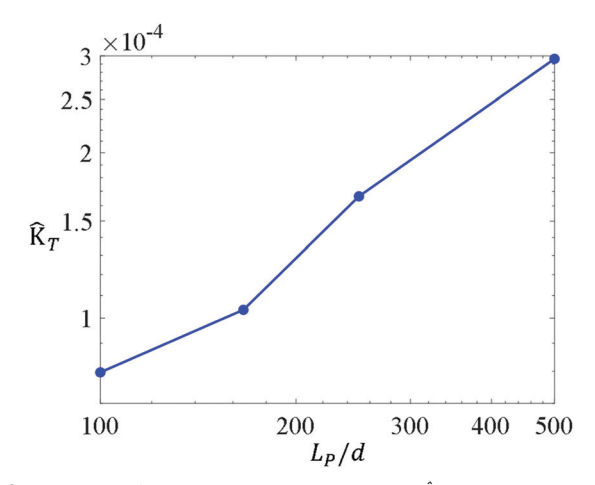


Fig. 8 Variation of the strain hardening modulus \hat{K}_T in regime II with the fiber persistence length, L_P . Note that this increase of \hat{K}_T as fibers become less tortuous is not a result of gradual pulling out of crimp, which becomes dominant only in regime III and in networks of infinite fibers.

The dependence of the stress–strain curve on the fiber persistence length parameter, $L_{\rm P}$, shown in Fig. 5(b) can be understood along the same lines. Fig. 6(c) and (d) show the variation of $N_{\rm a}$ and \bar{s} during the deformation of networks with various $L_{\rm P}$ and the same $\Psi_{\rm N}^{\rm Adh}$ and $\Psi_{\rm T}^{\rm Fric}$. We observe that $N_{\rm a}$ is independent of $L_{\rm P}$ (Fig. 6(c)), while $d\bar{s}/d\varepsilon_{\rm xx}$ increases continuously with increasing $L_{\rm P}$ (Fig. 6(d)) – a situation opposite to that observed when $\Psi_{\rm T}^{\rm Fric}$ is varied at constant $L_{\rm P}$. This indicates that, based on eqn (7), $\hat{K}_{\rm T}$ should increase with $L_{\rm P}$. This function is shown in Fig. 8. Furthermore, \bar{s} at yield increases with increasing $L_{\rm P}$ (Fig. 6(d)), while $N_{\rm a}$ is independent of $L_{\rm P}$ (Fig. 6(c)). Based on eqn (6), it is observed that the yield stress should increase with increasing $L_{\rm P}$, which justifies the trend observed in Fig. 5(b).

3.4 Contacts with stochastic properties in mats of infinite wavy fibers

In the previous section it is assumed that all contacts in a given model have identical $\Psi_{\rm N}^{\rm Adh}$ and $\Psi_{\rm T}^{\rm Fric}$. Since this is not the case in realistic mats, it is of interest to investigate the effect of

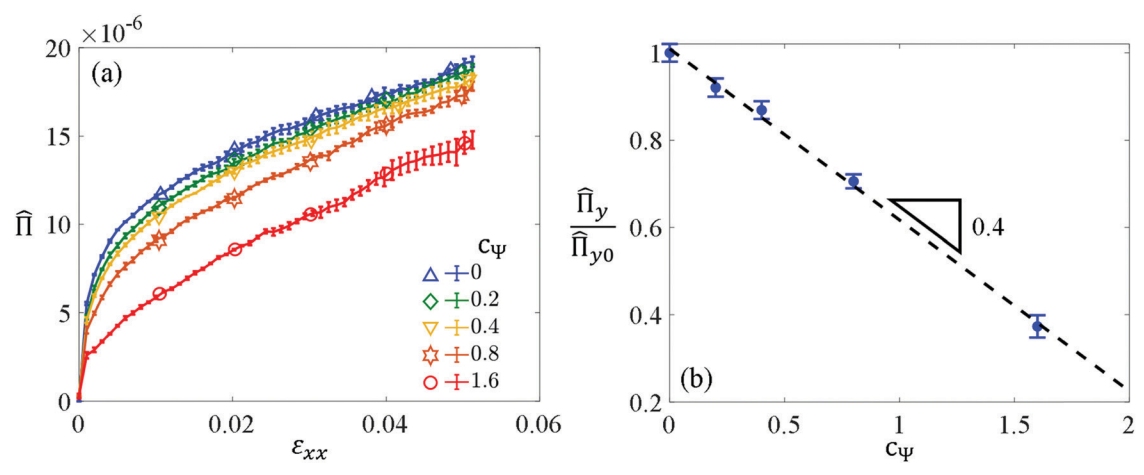


Fig. 9 (a) Stress-strain curves for networks with stochastic $\Psi_{T}^{\rm Fric}$, for increasing coefficient of variation of $\Psi_{T}^{\rm Fric}$, c_{Ψ} , and at constant mean of the respective distribution, $\bar{\Psi}_{T}^{\rm Fric}$ (b) Variation of the yield stress of the curves in (a) with c_{Ψ} .

stochasticity of contact properties on the stress–strain response. For this purpose, $\Psi_{\rm T}^{\rm Fric}$ for each contact in the model is sampled from a Gamma distribution with a specified mean, $\bar{\Psi}_{\rm T}^{\rm Fric}$, and a coefficient of variation, c_{Ψ} (also characterized by shape parameter $(S_{\rm sp})$ and scale parameter $(S_{\rm sc})$). $\Psi_{\rm N}^{\rm Adh}$ was taken to be identical at all contacts. Case III type networks are chosen for this analysis, with $\Psi_{\rm N}^{\rm Adh} = \bar{\Psi}_{\rm T}^{\rm Fric} = 2.5 \times 10^{-5}$. The coefficient of variation of $\Psi_{\rm T}^{\rm Fric}$, c_{Ψ} , is varied in the interval (0, 1.6). Alternatively, $S_{\rm sp}$ is in the range of $(0.39, \infty)$ and $S_{\rm sc}/\bar{\Psi}_{\rm T}^{\rm Fric}$ is in the range of (0, 2.56) respectively.

Fig. 9(a) shows the stress–strain responses for various c_{Ψ} values. The yield stress $\hat{\Pi}_y$ decreases as c_{Ψ} increases, while $\hat{K}_{\rm T}$ is unaffected. Fig. 9(b) shows the variation of $\hat{\Pi}_y$ with c_{Ψ} indicating that $\hat{\Pi}_y \sim 1-0.4c_{\Psi}$. In various other systems with stochastic microstructures, it is observed that system-scale properties decrease with increasing magnitude of fluctuations of local material properties. The effective yield stress of a continuum with spatially fluctuating local yield stress values decreases upon increasing the amplitude of these fluctuations. ^{57,58} The stiffness of crosslinked networks of fibers of non-identical elastic properties also decreases as the variability of fiber properties increases. ⁴⁰ This applies to various types of continua, as discussed in ref. 59. Likewise, the strength of crosslinked networks in which the crosslink strength is sampled from a distribution decreases as the coefficient of variation of the distribution increases, while its mean is kept constant. ⁶⁰

We also considered networks in which Ψ_N^{Adh} is stochastic, while Ψ_T^{Fric} is identical at all contacts. We observe that fluctuations of Ψ_N^{Adh} have no effect on the stress–strain curve, which is identical to that of a system of homogeneous friction and adhesion with Ψ_N^{Adh} being equal to the mean of the distribution of Ψ_N^{Adh} values of the stochastic case.

3.5 Effect of elliptical contacts in mats of infinite wavy fibers

A key assumption of the analysis presented in the previous sections is that contacts are circular. This implies that Ψ_N^{Adh} and Ψ_T^{Fric} are independent of the inter-fiber angle (θ) (see the inset

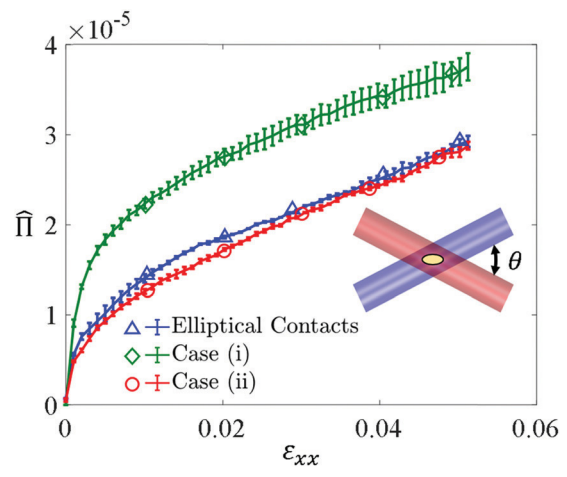


Fig. 10 Stress—strain curves for networks with elliptical contacts and for cases (i) and (ii) described in the text.

to Fig. 10). Since two cylinders establish elliptical contacts of area dependent on the angle between the cylinder axes, it is important to evaluate the error introduced in the present models by ignoring this geometric feature. To this end, we allow contacts to be elliptical if $\theta < 90^{\circ}$. The elliptical contact model used is based on the approximation of JKR contacts described in ref. 61 and 62. The curvatures of the contact surface at the major and minor semi-axes is $R' = 0.5d/(1 - \cos \theta)$ and $R'' = 0.5d/(1 + \cos \theta)$. We combine R' and R'' to calculate an equivalent radius of curvature $R_e = \sqrt{R'R''} = 0.5d/\sin\theta$, which is assigned to an equivalent circular contact. 61,62 Using this radius in the standard JKR model of circular contact area, we obtain the normal separation force (scales linear with R_e) and the area of the contact (scales as $R_e^{4/3}$).⁴⁶ According to the friction model used in this work, the friction force is proportional to the contact area. Hence, the θ -dependent Ψ_{N}^{Adh} and Ψ_{T}^{Fric} become:

$$\Psi_{N}^{Adh}(\theta) = \breve{\Psi}_{N}^{Adh}/\sin\theta$$
 (10a)

$$\Psi_{\rm T}^{\rm Fric}(\theta) = \breve{\Psi}_{\rm T}^{\rm Fric} / (\sin \theta)^{4/3}$$
 (10b)

where $\check{\Psi}_N^{\text{Adh}}$ and $\check{\Psi}_T^{\text{Fric}}$ are the normalized normal and tangential separation forces at $\theta=90^\circ$. The analysis in ref. 61 and 62 indicates that this method leads to errors in the contact separation force on the order of 20% to 30% for R''/R' as high as 25. Furthermore, in order to prevent the unphysical divergence of expressions (10) when θ is small, we assign the values corresponding to $\theta=10^\circ$ to all contacts formed by fibers crossing at angles smaller than 10° . The analysis was performed using case III type networks with $\check{\Psi}_N^{\text{Adh}} = \check{\Psi}_T^{\text{Fric}} = 2.5 \times 10^{-5}$.

We observe that the structure of mats (defined by $l_{\rm c}$ and $h/\rho d^2$, Fig. 4(b)) with elliptical contacts of variable $\Psi_{\rm N}^{\rm Adh}(\theta)$ (eqn (10a)) is identical to that of mats of circular contacts and identical $\Psi_{\rm N}^{\rm Adh}$ set equal to the mean of the $\Psi_{\rm N}^{\rm Adh}(\theta)$ distribution. This result is identical to that noted in Section 3.4.

Furthermore, we compare the stress–strain curves of mats with elliptical contacts of parameters described by eqn (10), with that of geometrically identical mats with circular contacts and with either: (case I) $\Psi_{\rm N}^{\rm Adh}$ set equal to the mean of $\Psi_{\rm N}^{\rm Fric}(\theta)$, and $\Psi_{\rm T}^{\rm Fric}$ set equal to the mean of $\Psi_{\rm N}^{\rm Fric}(\theta)$ (circular contacts of identical properties), and (case II) $\Psi_{\rm N}^{\rm Adh}$ set equal to the mean of $\Psi_{\rm N}^{\rm Adh}(\theta)$, and $\Psi_{\rm T}^{\rm Fric}$ rendered stochastic and θ -independent, with its mean and coefficient of variation c_{Ψ} equal to the mean and the coefficient of variation of $\Psi_{\rm T}^{\rm Fric}(\theta)$. Fig. 10 shows the stress–strain curves for these three cases. It is seen that the model with elliptical contacts behaves identically to case II in which contacts are circular, but has stochastic properties. In agreement with the results presented in Section 3.4, neglecting the stochasticity of contact properties leads to an increase of the yield stress, but to no variation of regime II strain hardening, $\hat{K}_{\rm T}$.

3.6 Tensile response of mats with finite length wavy fibers

In this section, we consider networks of finite length wavy fibers corresponding to types VII and VIII, Table 1. The contour fiber length is set at $L_{\rm f} = 250d$. To limit size effects, the domain size is taken three times larger than $L_{\rm f}$ ($L_{\rm D} = 3L_{\rm f}$). $\Psi_{\rm N}^{\rm Adh} = 2.5 \times 10^{-4}$ in all

cases and $\Psi_{\rm T}^{\rm Fric}$ is varied. As in the case of infinite fibers (Section 3.3), the circular contact model with no variability is selected for this study. In models corresponding to type VII networks, $L_{\rm P} = L_{\rm f} = 250d$, while in type VIII networks, fibers are straight, with $L_{\rm P} = \infty$.

Stress–strain curves for type VIII networks of finite length straight fibers with various $\Psi_{\rm T}^{\rm Fric}$ values but the same $\Psi_{\rm N}^{\rm Adh}$ are shown in Fig. 11(a). All networks undergo localization immediately after entering regime II and the load carrying capacity reduces gradually over a prolonged post-localization regime. This is the stabilizing consequence of inter-fiber friction. Fig. 11(b) shows the peak stress of the curves in Fig. 11(a), *i.e.* the network strength, $\hat{\Pi}_{\rm f}$, function of $\Psi_{\rm T}^{\rm Fric}$. A linear relation between these two quantities emerges, which is a result of the frictional nature of stress in these networks. It is of interest to observe that in crosslinked networks that fail due to crosslink rupture, the strength of the network is also proportional to the strength of the crosslinks, as observed in numerical 60,63 and experimental 64 studies.

The effect of the persistence length $L_{\rm P}$ is shown in Fig. 12. Case VII and case VIII networks are considered, having the same contact properties, $\Psi_{\rm N}^{\rm Adh}=2.5\times10^{-4}$ and $\Psi_{\rm T}^{\rm Fric}=2.5\times10^{-5}$, the same $L_{\rm f}$, and the same density $\rho d=0.48$ (Table 1). The case VII networks have finite $L_{\rm P}$, while case VIII networks have straight fibers. The stress–strain curve of the mat with straight fibers has a well-defined peak corresponding to strain localization. The peak moves to larger strains, and it is less pronounced (localization is more diffuse) in the case of wavy fibers. Based on the post-localization response, it can be stated that the mat with straight fibers is more brittle compared to that with wavy fibers, with more energy being dissipated in the second case. A similar stress–strain response for finite length straight fiber networks was also observed in ref. 30.

The kinematics of these networks is based on two main mechanisms: straightening of wavy fibers and fiber pull-out. The mechanics of straightening of wavy fibers is identical to that discussed for mats of infinite wavy fibers. The gradual removal of fiber slack during straining leads to some level of strain stiffening (non-zero \hat{K}_T). Slip at consecutive contacts along given fiber is largely uncorrelated when waviness is pronounced. As fibers

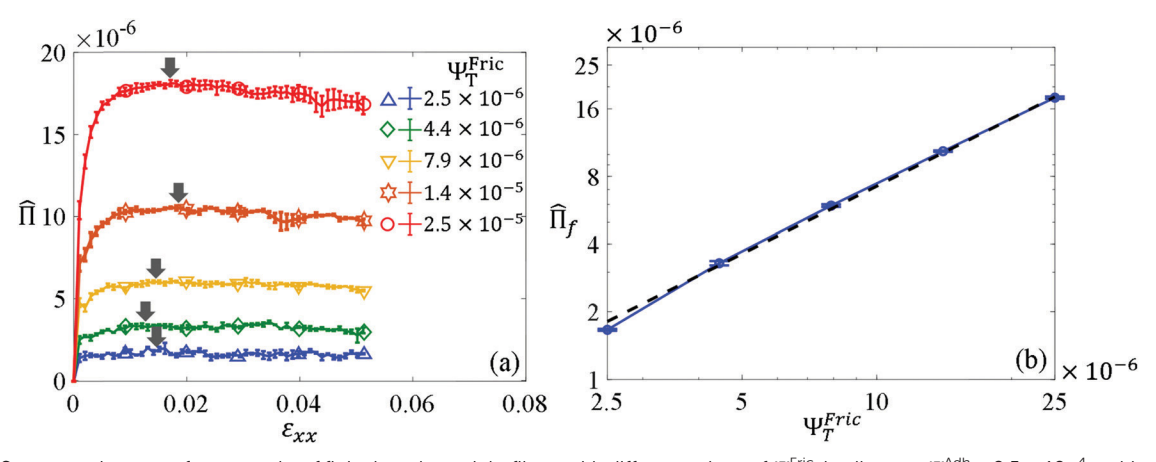


Fig. 11 (a) Stress-strain curves for networks of finite length, straight fibers with different values of Ψ_{T}^{Fric} . In all cases, $\Psi_{N}^{Adh} = 2.5 \times 10^{-4}$ and $L_{P} = L_{f} = 250d$. Arrows indicate the peak stress. (b) Variation of the peak stress with Ψ_{T}^{Fric} . The bars represent the standard error of 3 realizations.

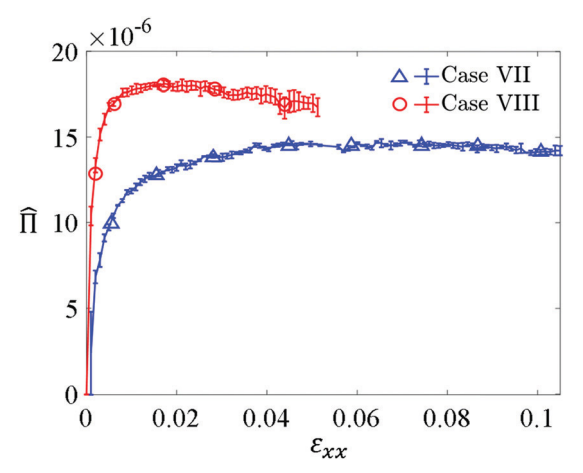


Fig. 12 Stress-strain curves for networks of straight (case VIII) and wavy (case VII) fibers of finite length and the same friction and adhesion parameters.

straighten, axial stress develops gradually. Since this is an energetically unfavorable mode, fiber pullout and consequently, localization may follow. The resistance to fiber pullout depends on the total number of contacts per fiber and $\Psi_{\rm T}^{\rm Fric}$. Straight chopped fibers have no slack and therefore accommodate strain only through fiber pullout which explains the localization at small strains. Thus, fiber waviness delays strain localization thereby rendering the network more ductile.

4. Conclusions

Adhesion in quasi-2D mat-like networks of fibers determines their structure and mechanical properties. In such adhesion-stabilized networks, power laws are established between the mean contour length between contacts, the network thickness, and the strength of adhesion. Fiber tortuosity has little effect on the structural parameters such as the mean contour length between contacts and the network thickness.

The effect of fiber tortuosity, adhesion, and friction on the tensile mechanical response of these networks is discussed. It is shown that mechanics is controlled by frictional dissipation rather than by the variation of the strain energy during deformation. The stress-strain response is, in general, bi-linear. The post-yielding strain hardening modulus increases with increasing friction sub-linearly. It is found that the deviation from the expected linear relation is due to a decrease in the number of actively slipping contacts with increasing tangential contact separation force. Normal contact separation force affects the tangent stiffness by increasing the total number of contacts in the network. Strain hardening also increases upon increasing the persistence length of the fibers. It is shown that variability in normal and tangential contact separation forces does not affect the mat structure or the degree of strain hardening. However, the yield stress decreases with increasing variability of the tangential contact separation force at contacts.

If fibers are of finite length, strain localization occurs at a critical strain which decreases with increasing fiber tortuosity.

Finite length straight fibers show no post-yield strain hardening and undergo strain localization shortly after yielding. Thus, tortuosity in fibrous mats with adhesion and friction renders the network more ductile.

This work provides guidelines for designing fibrous mats with desired mechanical properties by controlling the fiber tortuosity, contact adhesion and friction. These data are expected to be of importance for the design of electrospun mats for bioengineered tissues, spun fibrous materials for various consumer products and geotextiles, and other applications in biology and engineering.

Conflicts of interest

There are no conflicts to declare.

Appendix

Consider an angularly restricted correlated random walk of step length l_s , as shown in Fig. 13. The angular deviation between consecutive steps i and i+1, i.e. $\Delta\theta_i = \cos^{-1}(n_i.n_{i+1})$, where n_i , which denotes the direction of the walk at step i, is sampled from a uniform distribution in the interval $(-\alpha,\alpha)$. The directional spatial auto-correlation, C_{θ} , needs to be found, as a function of the number of steps, n, in order to calculate the persistence length, L_P .

$$C_{\theta}(n) = \mathbb{E}\left(\cos\left(\sum_{i=1}^{n} \Delta\theta_{i}\right)\right)$$
 (A1)

where E() is the expectation function, and $\Delta\theta_i$ is sampled from a uniform distribution in the interval $(-\alpha,\alpha)$. The distribution has mean zero and variance $\alpha^2/3$. $\sum_{i=1}^n \Delta\theta_i$ forms an Irwin-Hall distribution. This distribution between converges to the normal

distribution. This distribution, however, converges to the normal distribution rapidly with increasing n. The mean of the normal distribution approximating the Irwin–Hall distribution for large enough n (the approximation is already quite good at n = 10) is zero and its variance is $n\alpha^2/3$.

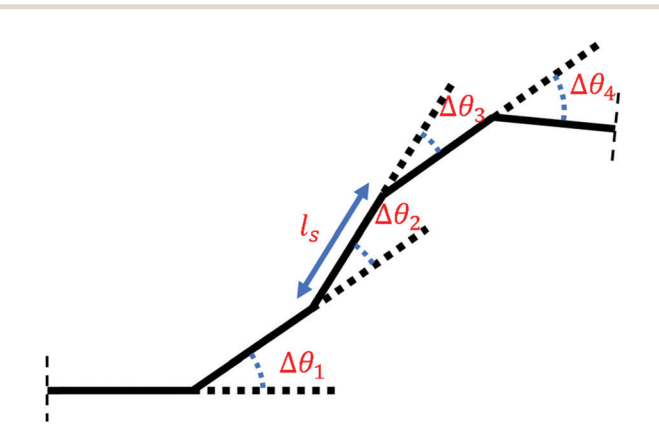


Fig. 13 Schematic showing the angularly restricted correlated random walk

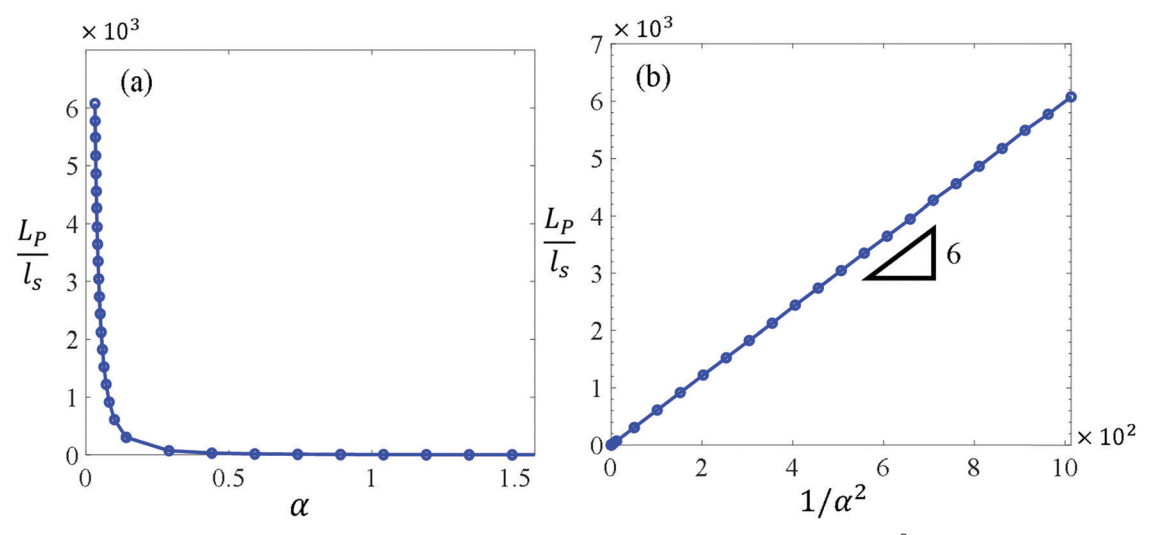


Fig. 14 (a) Numerical evaluation of the normalized persistence length L_P/I_s vs. α . (b) Data in (a) replotted vs. $1/\alpha^2$ (symbols) along with the prediction of eqn (A4) (line) demonstrating the validity of the results derived in this Appendix for this range of α .

The expectation of cos(X) for X being sampled from a normal distribution, $\aleph(0, \sigma^2)$, where σ^2 is the variance is:

$$E(X) = e^{-\frac{\sigma^2}{2}} \tag{A2}$$

Substituting $\sigma^2 = n\alpha^2/3$ in eqn (A2) provides the desired approximation of (A1):

$$C_{\theta}(n) = E\left(\cos\left(\sum_{i=1}^{n} \Delta\theta_{i}\right)\right) \approx e^{-\frac{n}{6/\alpha^{2}}}$$
 (A3)

where n is the number of steps or l/l_s (l is the contour length of the path).

The persistence length, L_P , is approximated by fitting $\exp(-l/L_P)$ (or $\exp(-n/(L_P/l_s))$) to the directional spatial autocorrelation function, $C_\theta(n)$. From, eqn (A3) it can be concluded that

$$L_{\rm P}/l_{\rm s} \approx 6/\alpha^2$$
. (A4)

Fig. 14(a) shows $L_{\rm P}/l_{\rm s}$ evaluated numerically for various values of α . The data are replotted in Fig. 14(b) as $L_{\rm P}/l_{\rm s}$ vs. $1/\alpha^2$ (symbols) to demonstrate the level of accuracy of eqn (A4) represented by the line.

Acknowledgements

This work was supported by the National Science Foundation through grant No. CMMI-1634328.

References

- C. P. Broedersz and F. C. Mackintosh, *Rev. Mod. Phys.*, 2014, 86, 995–1036.
- 2 R. C. Picu, Soft Matter, 2011, 7, 6768-6785.
- 3 W.-J. Li, C. T. Laurencin, E. J. Caterson, R. S. Tuan and F. K. Ko, *J. Biomed. Mater. Res.*, 2002, **60**, 613–621.
- 4 J. B. Carleton, A. D'Amore, K. R. Feaver, G. J. Rodin and M. S. Sacks, *Acta Biomater.*, 2015, **12**, 93–101.

- 5 P. H. G. Chao, H. Y. Hsu and H. Y. Tseng, *Biofabrication*, 2014, 6, 035008.
- 6 M. C. McManus, E. D. Boland, H. P. Koo, C. P. Barnes, K. J. Pawlowski, G. E. Wnek, D. G. Simpson and G. L. Bowlin, *Acta Biomater.*, 2006, 2, 19–28.
- 7 Q. P. Pham, U. Sharma and A. G. Mikos, *Tissue Eng.*, 2006, 12, 1197–1211.
- 8 S. S. Choi, S. G. Lee, C. W. Joo, S. S. Im and S. H. Kim, J. Mater. Sci., 2004, 39, 1511–1513.
- 9 C.-L. Pai, M. C. Boyce and G. C. Rutledge, *Polymer*, 2011, 52, 6126–6133.
- 10 S. C. Wong, A. Baji and S. Leng, Polymer, 2008, 49, 4713-4722.
- 11 X. Fang, S. Xiao, M. Shen, R. Guo, S. Wang and X. Shi, *New J. Chem.*, 2011, 35, 360–368.
- 12 A. J. Benítez and A. Walther, *J. Mater. Chem. A*, 2017, 5, 16003–16024.
- 13 R. Mao, N. Meng, W. Tu and T. Peijs, *Cellulose*, 2017, **24**, 4627–4639.
- 14 M. Henriksson, L. A. Berglund, P. Isaksson, T. Lindström and T. Nishino, *Biomacromolecules*, 2008, **9**, 1579–1585.
- 15 H. Zhu, S. Zhu, Z. Jia, S. Parvinian, Y. Li, O. Vaaland, L. Hu and T. Li, *Proc. Natl. Acad. Sci. U. S. A.*, 2015, **112**, 8971–8976.
- 16 A. J. Benítez, J. Torres-Rendon, M. Poutanen and A. Walther, Biomacromolecules, 2013, 14, 4497–4506.
- 17 M. N. Silberstein, C.-L. Pai, G. C. Rutledge and M. C. Boyce, *J. Mech. Phys. Solids*, 2011, **60**, 295–318.
- 18 B. M. Baker, N. L. Nerurkar, J. A. Burdick, D. M. Elliott and R. L. Mauck, *J. Biomech. Eng.*, 2009, 131, 101012.
- 19 S. Domaschke, M. Zündel, E. Mazza and A. E. Ehret, *Int. J. Solids Struct.*, 2019, **158**, 76–89.
- 20 M. Zündel, E. Mazza and A. E. Ehret, *Soft Matter*, 2017, **13**, 6407–6421.
- 21 S. Goutianos, R. Mao and T. Peijs, *Int. J. Solids Struct.*, 2018, **136–137**, 271–278.
- 22 Y. Liu and Y. Dzenis, Micro Nano Lett., 2016, 11, 727-730.
- 23 S. Toll and J.-A. E. Manson, J. Appl. Mech., 1995, 62, 223.

- 24 C. M. van Wyk, J. Text. Inst., Trans., 1946, 37, T285-T292.
- 25 T. Komori and K. Makishima, Text. Res. J., 1977, 47, 13-17.
- 26 D. Poquillon, B. Viguier and E. Andrieu, *Journal of Materials Science*, Kluwer Academic Publishers, 2005, vol. 40, pp. 5963–5970.
- 27 J. Schofield, J. Text. Inst., Trans., 1938, 29, T239-T252.
- 28 D. Rodney, M. Fivel and R. Dendievel, *Phys. Rev. Lett.*, 2005, **95**, 2–5.
- 29 G. Subramanian and C. R. Picu, Phys. Rev. E: Stat., Non-linear, Soft Matter Phys., 2011, 83, 056120.
- 30 A. Kulachenko and T. Uesaka, Mech. Mater., 2012, 51, 1-14.
- 31 M. Endo, H. Muramatsu, T. Hayashi, Y. A. Kim, M. Terrones and M. S. Dresselhaus, *Nature*, 2005, **433**, 476.
- 32 S. Yunoki, H. Hatayama, M. Ebisawa, E. Kondo and K. Yasuda, *J. Biomed. Mater. Res., Part A*, 2015, **103**, 3054–3065.
- 33 M. Tempel, G. Isenberg and E. Sackmann, *Phys. Rev. E: Stat. Phys., Plasmas, Fluids, Relat. Interdiscip. Top.*, 1996, 54, 1802–1810.
- 34 R. C. Picu and A. Sengab, Soft Matter, 2018, 14, 2254-2266.
- 35 V. Negi and R. C. Picu, J. Mech. Phys. Solids, 2019, 122, 418-434.
- 36 A. Sengab and R. C. Picu, Phys. Rev. E, 2018, 97, 032506.
- 37 T. Ushiki, Arch. Histol. Cytol., 2002, 65, 109–126.
- 38 V. H. Barocas, A. M. Kerandi, C. R. Frey, R. T. Tranquillo, V. K. Lai and S. P. Lake, *Acta Biomater.*, 2012, 8, 4031–4042.
- 39 A. Kabla and L. Mahadevan, *J. R. Soc., Interface*, 2007, 4, 99–106.
- 40 E. Ban, V. H. Barocas, M. S. Shephard and C. R. Picu, J. Appl. Mech., 2016, 83, 041008.
- 41 J. Howard, *Mechanics of motor proteins and the cytoskeleton*, Sinauer Associates, Publishers, 2001.
- 42 T. van Dillen, P. R. Onck and E. Van der Giessen, *J. Mech. Phys. Solids*, 2008, **56**, 2240–2264.
- 43 D. A. Head, A. J. Levine and F. C. MacKintosh, *Phys. Rev. Lett.*, 2003, **91**, 108102.
- 44 J. Wilhelm and E. Frey, Phys. Rev. Lett., 2003, 91, 108103.

- 45 B. V. Derjaguin, V. M. Muller and Y. P. Toporov, *Prog. Surf. Sci.*, 1994, **45**, 131–143.
- 46 K. L. Johnson, K. Kendall and A. D. Roberts, *Proc. R. Soc. A Math. Phys. Eng. Sci.*, 1971, 324, 301–313.
- 47 Q. Shi, K. T. Wan, S. C. Wong, P. Chen and T. A. Blackledge, *Langmuir*, 2010, **26**, 14188–14193.
- 48 Q. Shi, S. C. Wong, W. Ye, J. Hou, J. Zhao and J. Yin, *Langmuir*, 2012, **28**, 4663–4671.
- 49 F. P. Bowden and D. Tabor, *The friction and lubrication of solids*, Oxford University Press, 2001, vol. 1.
- 50 A. M. Homola, J. N. Israelachvili, P. M. Mcguiggan and M. L. Gee, *Wear*, 1990, **136**, 65–83.
- 51 R. W. Carpick, N. Agraït, D. F. Ogletree and M. Salmeron, *Langmuir*, 1996, **12**, 3334–3340.
- 52 M. P. Allen and D. J. Tildesley, *Computer simulation of liquids*, Clarendon Press, 1987.
- 53 L. M. Pritykin, J. Colloid Interface Sci., 1986, 112, 539-543.
- 54 O. J. Kallmes and H. Corte, Tappi J., 1960, 43, 737-752.
- 55 S. Toll, Polym. Eng. Sci., 1998, 38, 1337-1350.
- 56 G. Zagar, P. R. Onck and E. Van Der Giessen, *Biophys. J.*, 2015, **108**, 1470–1479.
- 57 V. Negi and R. C. Picu, Mech. Mater., 2018, 120, 26-33.
- 58 R. C. Picu, S. Sorohan, M. A. Soare and D. M. Constantinescu, *Mech. Mater.*, 2016, **97**, 59–66.
- 59 E. Ban, Mech. Mater., 2019, 129, 139-147.
- 60 S. Deogekar and R. C. Picu, J. Mech. Phys. Solids, 2018, 116, 1–16.
- 61 N. H. M. Zini, M. B. de Rooij, M. Bazr Afshan Fadafan, N. Ismail and D. J. Schipper, *Tribol. Lett.*, 2018, **66**, 30.
- 62 K. L. Johnson and J. A. Greenwood, *J. Phys. D: Appl. Phys.*, 2005, **38**, 1042–1046.
- 63 S. Heyden, Network Modelling for the Evaluation of Mechanical Properties of Cellulose Fluff, 2000, vol. PhD.
- 64 J. Forsström, A. Torgnysdotter and L. Wågberg, *Nord. Pulp Pap. Res. J.*, 2005, 20, 186–191.